Materials Today Advances 20 (2023) 100422

Contents lists available at ScienceDirect

Materials Today Advances

journal homepage: www.journals.elsevier.com/materials-today-advances/

Formation of quaternary $Zn(Al_xGa_{1-x})_2O_4$ epilayers driven by thermally induced interdiffusion between spinel $ZnGa_2O_4$ epilayer and Al_2O_3 substrate

Samiran Bairagi [a], Jui-Che Chang [a], Fu-Gow Tarntair [b], Wan-Yu Wu [c], Gueorgui K. Gueorguiev [a], Edward Ferraz de Almeida Jr. [e], Roger Magnusson [a], Kun-Lin Lin [d], Shao-Hui Hsu [d], Jia-Min Shieh [d], Jens Birch [a], Ray-Hua Horng [b,*], Kenneth Järrendahl [a], Ching-Lien Hsiao [a,**]

[a] Thin Film Physics Division, Department of Physics, Chemistry and Biology (IFM), Linköping University, SE-581 83, Linköping, Sweden
[b] Institute of Electronics, National Yang Ming Chiao Tung University, Hsinchu, 30010, Taiwan
[c] Department of Materials Science and Engineering, National United University, Miaoli, 36063, Taiwan
[d] Taiwan Semiconductor Research Institute (TSRI), National Applied Research Laboratories, Hsinchu, 30091, Taiwan
[e] Federal University of the West of Bahia, Center for Exact Sciences and Technologies, Rua Bertioga, 892, Morada Nobre I, CEP: 47810-059, Barreiras, BA, Brazil

ARTICLE INFO

Keywords:
Zinc aluminogallate
Ellipsometry
Semiconductors
Annealing
Interdiffusion
Bandgap

ABSTRACT

Zinc aluminogallate, $Zn(Al_xGa_{1-x})_2O_4$ (ZAGO), a single-phase spinel structure, offers considerable potential for high-performance electronic devices due to its expansive compositional miscibility range between aluminum (Al) and gallium (Ga). Direct growth of high-quality ZAGO epilayers however remains problematic due to the high volatility of zinc (Zn). This work highlights a novel synthesis process for high-quality epitaxial quaternary ZAGO thin films on sapphire substrates, achieved through thermal annealing of a $ZnGa_2O_4$ (ZGO) epilayer on sapphire in an ambient air setting. *In-situ* annealing x-ray diffraction measurements show that the incorporation of Al in the ZGO epilayer commenced at 850 °C. The Al content (x) in ZAGO epilayer gradually increased up to around 0.45 as the annealing temperature was raised to 1100 °C, which was confirmed by transmission electron microscopy (TEM) and energy dispersive x-ray spectroscopy. X-ray rocking curve measurement revealed a small full width at half maximum value of 0.72 °, indicating the crystal quality preservation of the ZAGO epilayer with a high Al content. However, an epitaxial intermediate β –$(Al_xGa_{1-x})_2O_3$ layer (β - AGO) was formed between the ZAGO and sapphire substrate. This is believed to be a consequence of the interdiffusion of Al and Ga between the ZGO thin film and sapphire substrate. Using density functional theory, the substitution cost of Ga in sapphire was determined to be about 0.5 eV lower than substitution cost of Al in ZGO. Motivated by this energetically favorable substitution, a formation mechanism of the ZAGO and AGO layers was proposed. Spectroscopic ellipsometry studies revealed an increase in total thickness of the film from 105.07 nm (ZGO) to 147.97 nm (ZAGO/AGO) after annealing to 1100 °C, which were corroborated using TEM. Furthermore, an observed increase in the direct (indirect) optical bandgap from 5.06 eV (4.7 eV) to 5.72 eV (5.45 eV) with an increasing Al content in the ZAGO layer further underpins the formation of a quaternary ZAGO alloy with a tunable composition.

1. Introduction

In the pursuit of high-performance semiconducting materials with wide bandgaps and high thermal stability, researchers have long been exploring alternative candidates for various technological applications. Two materials that have garnered significant attention in this area are zinc gallate ($ZnGa_2O_4$) and β - gallium oxide ($\beta - Ga_2O_3$), known for their ultra-wide bandgap and high breakdown voltage. $ZnGa_2O_4$ has a face-centered-cubic AB_2O_4 spinel structure with $Fd\bar{3}m$ space group symmetry in which Zn^{2+} ions occupy the tetrahedral A-sites and Ga^{3+} ions occupy the octahedral B-sites. It has recently been considered as a

* Corresponding author.
** Corresponding author.
E-mail addresses: rayhua@nycu.edu.tw (R.-H. Horng), ching-lien.hsiao@liu.se (C.-L. Hsiao).

https://doi.org/10.1016/j.mtadv.2023.100422
Received 1 July 2023; Received in revised form 28 August 2023; Accepted 6 September 2023
Available online 13 September 2023

next generation semiconductor material and received increasing attention from researchers. Its ultra-wide bandgap and high breakdown voltage make it suitable for an array of applications including field effect transistors, Schottky-barrier diode, deep ultraviolet photodetector, phosphor, electroluminescent devices memory device, and sensors [1,2]. $\beta - Ga_2O_3$ has a base-centered monoclinic lattice belonging to space group 12. It has also attracted significant attention in high power electronic devices thanks to its feasibility with n-type doping, high predicted breakdown electric fields and high Baliga's figure of merit over popular current generation materials such as SiC and GaN [3–6].

Yet, it is essential to recognize that the scope of these applications can be considerably broadened using bandgap engineering, which has not yet been investigated in detail for these materials. Engineering the bandgap of semiconductor materials is potentially desirable for material design flexibility and application in various devices. For Ga_2O_3, alloying it with Al_2O_3 by direct growth of $(Al_xGa_{1-x})_2O_3$ thin film (AGO) has been investigated using mist chemical vapor deposition (CVD) [6], pulsed laser deposition (PLD) [7], sputtering [8], molecular beam epitaxy (MBE) [9,10], and metalorganic chemical vapor deposition (MOCVD) [11,12]. Among them, high-quality AGO[3] epitaxial layers have primarily been grown using MBE and MOCVD. A thermal-induced diffusion of aluminum from sapphire substrate to Ga_2O_3 for the formation of AGO during post annealing has also been considered as a strategy to widen the bandgap [13–15]. Goyal et al. observed that the bandgap of $\beta - Ga_2O_3$ increased from 4.63 to 5.15 eV after a 1000 $^\circ C$ annealing for 36 h [16]. Wuu et al. reported that the bandgap of $\beta - Ga_2O_3$ gradually increased from 4.95 to 5.33 eV for furnace-annealed film and 4.95–5.00 eV for rapid thermal annealing treated film when the temperature increased from 700 to 1000 $^\circ C$ [17]. Liao et al. tuned the optical bandgap of $\beta - Ga_2O_3$ from 5.31 to 6.38 eV with 72% of Al after 3 h of annealing at temperatures from 1000 to 1400 $^\circ C$ [3]. Singh et al. reported a $\beta - Ga_2O_3$ exhibiting larger bandgaps (between 5.15 and 5.17 eV) by annealing at the film at 1000 $^\circ C$ in O_2 atmosphere for 120 min [18]. It is evident from these works that thermally induced interdiffusion could be considered a low cost and straightforward method to engineer the bandgaps of these materials.

In this context, quaternary $Zn(Al_xGa_{1-x})_2O_4$ alloy (ZAGO)[1] can be considered as an alternative promising candidate for high-performance electronic devices especially due to its ease of synthesis into a single-phase spinel structure. Thanks to the expansive compositional miscibility range between Al and Ga, ZAGO offers exceptional versatility in bandgap tuning which is essential for applications demanding precise control over electronic and optical properties. It maintains its cubic spinel structure even at higher temperatures, avoiding phase transitions that could lead to defects, interface states, or mechanical strains, which is vital for ensuring long-term device stability and performance. This stands in contrast to alloying $\beta - Ga_2O_3$ (which has a stable monoclinic structure), with Al_2O_3 (which has a stable rhombohedral or hexagonal structure) as it may induce unexpected phase transitions, which could be disadvantageous. Moreover, the thermally induced interdiffusion method for bandgap engineering remains largely unexplored for ZAGO, thus offering an exciting avenue for future research.

Materials being proposed for high power applications could benefit from studies on the evolution of their structural and optical properties when exposed to elevated temperatures. However not many studies have discussed these properties for $ZnGa_2O_4$ (ZGO)[2] being exposed to high temperatures or the effect of interdiffusion with its substrate. Hilfiker et al. have recently reported the dielectric function and interband transitions of melt grown ZGO for temperatures up to 600 $^\circ C$, where they observed a decrease in bandgap at a slope of -0.72 meVK^{-1} with increasing temperatures [19]. Wang et al. studied radio frequency sputtered ZGO thin films on sapphire for temperatures ranging from 500 to 900 $^\circ C$. They observed an increase in bandgap energy from 4.7 eV to 4.98 eV and improvement in crystal quality with increase in temperature [20].

In this work, we use high temperature thermal annealing to modulate the bandgap of high crystal quality ZGO thin films, leading to the formation of ZAGO and assess its implications on the structural and optical properties. The crystal quality and epitaxial relationship of both films with the substrate is determined using X-ray diffraction (XRD), X-ray rocking curve measurements (XRC) and high-resolution transmission electron microscopy (HRTEM), while the composition of the films is analyzed using energy dispersive X-ray spectroscopy (EDS) in TEM. The effect of interdiffusion with the sapphire substrate is addressed and the formation mechanism of quaternary ZAGO and ternary β - phase AGO is discussed based on formation energies and substitution costs using density function theory (DFT) modelling and calculations. Spectroscopic ellipsometry is used to determine the optical constants as well as the direct and indirect optical bandgaps of ZAGO. By elucidating the distinctive attributes of ZAGO, we aim to showcase its usefulness and potential towards advancements in power electronics and optoelectronic technologies.

2. Experimental and modeling details

The as-grown ZGO epitaxial thin films were grown on *c*-plane sapphire substrates at 750 $^\circ C$ by MOCVD at a growth pressure of 25 torr. Diethylzinc (DEZn), triethylgallium (TEGa) and oxygen were used as Zn, Ga and O_2 precursors, and the flow rates of precursors were maintained at 90, 100 and 700 sccm, respectively.

Both *in-situ* (during annealing) and *ex-situ* (after annealing) x-ray diffraction (XRD) measurement of the samples was performed to study the film crystal structure using a PANalytical Empyrean X-ray diffractometer (Malvern PANalytical, Almelo, The Netherlands) equipped with a heating stage. A Cu X-ray source was powered using a 45 kV generator voltage and 40 mA tube current. The primary optics comprised of a parabolic multilayer mirror followed by a 0.5 $^\circ$ divergence slit, and a 0.27 $^\circ$ parallel plate collimator was used as the secondary optics. A Ni foil was used to filter $Cu - K_\beta$ line. For the *in-situ* annealing study, a sample was heated directly from room temperature to 600 $^\circ C$ in 30 min, follow-up with temperatures ranging from 600 to 1100 $^\circ C$ (limit of the instrument) in air in steps of 50 $^\circ C$. The measurement was performed on the same sample at each temperature step of the annealing process. For the *ex-situ* annealing study, various samples cut from the same epiwafer were heated to the set-point temperatures of 750, 800, 950, and 1100 $^\circ C$ and kept for 30 min in air. The measurement was performed after samples were cooled down to room temperature.

The microstructural characterization of the reaction products was performed using a transmission electron microscope, TEM (JEM 2010Fx, JEOL Ltd., Tokyo, Japan) equipped with an energy dispersive spectrometer, EDS (Model ISIS300, Oxford Instrument Inc., London, U.K.). The Inorganic Crystal Structure Database (ICSD) and crystallographic software (Diamond version 3.0 and CaRIne Crystallography 3.1) were used for the identification of the crystal structures of the phases. The TEM specimens were prepared by focused ion beam (FEI Helios 1200+). The quantitative composition analyses were performed based on the principle of the Cliff-Lorimer standard-less method. The image magnification of TEM was calibrated using the MAG*I*CAL reference standard sample (Norrox Scientific Ltd., Beaver Pond, ON, Canada) to accurately calculate the lattice parameters of reaction products.

The framework adopted for modeling the structure and the energy costs for substitution of Al and Ga atoms (ions) in the compounds of interest for this work is the density functional theory (DFT) within its generalized gradient approximation (GGA) at the Perdew-Burke-Ernzerhof (PBE) level of theory as implemented in the Quantum Espresso code [21]. This implementation employs Plane-Wave basis sets and projector augmented wave method (PAW) pseudopotentials [22] for

[1] Zinc aluminogallate, $Zn(Al_xGa_{1-x})_2O_4$
[2] Zinc gallate, $ZnGa_2O_4$
[3] Aluminum gallate, $(Al_xGa_{1-x})_2O_3$

the aluminum, gallium, oxygen, and zinc atoms, respectively. Both $ZnGa_2O_4$ and $ZnAl_2O_4$ model systems contain 56 atoms per unit cell constructed under a cubic $Fd\bar{3}m$ space group. The formation energies of the studied compounds were calculated according to the expression:

$$E_{\text{form/at}} = \frac{E_{\text{tot}} - \sum n_i \mu_i}{\sum n_i} \quad (1)$$

whereby E_{tot} is the total energy per supercell of the corresponding material system. n_i (i = Zn, Al, Ga, O) represents the number of metal atoms Zn, Al, Ga whenever present in any of the modelled compounds, and the number of O atoms in the supercell, respectively. μ_i (i = Zn, Al, Ga, O), represents the chemical potentials of the metal atoms in the corresponding pure metals, and the chemical potential of the oxygen atom as obtained from the O_2 gas, respectively; all chemical potential values are calculated at the same level of theory (PBE) as used for the simulation of the ZGO, ZAGO, and AGO compounds.

Optical properties of as-grown and thermal annealed samples were measured and analyzed using a Mueller matrix spectroscopic ellipsometer (SE) with the CompleteEase software package, both from J. A. Woollam Co., Inc. (Lincoln, NE, USA). The measurements were made over a spectral range of 210–1690 nm (0.7–5.9 eV), at three angles of incidence (45 °, 55 ° and 65 °). Optical properties such as the complex refractive index (N) and absorption coefficient (α) as a function of photon energy (E) were obtained from model fitting of the ellipsometric data, while optical bandgap (E_g) values were evaluated by line shape analysis of α as a function of E. Morphological parameters such as surface roughness, thickness of film and thickness of intermediate layer were also determined as a result of the ellipsometric data analysis. Ellipsometric data analysis depends on the Fresnel reflection and transmission equations for polarized light. A ratio ρ of complex valued Fresnel reflection coefficients is used to define the standard ellipsometric parameters, ψ and Δ, expressed as,

$$\rho = r_p / r_s = tan(\psi) \cdot e^{i\Delta} \quad (2)$$

where, r_p and r_s represent complex valued p- and s-polarized reflectance coefficients from layered systems with plane-parallel interfaces, ψ indicates change in amplitudes in p- and s-polarized reflected light and Δ represents the difference in their phase.

3. Results and discussion

3.1. XRD measurement: in-situ and post annealing in air

The *in-situ* XRD measurements, including $\theta/2\theta$ scans and X-ray rocking curve (XRC) measurements of as-grown ZGO thin film on sapphire samples annealed in air are plotted in Fig. 1. The long range $\theta/2\theta$ XRD scans (2θ = 10 ° to 60 °) for all ZGO samples (one at room temperature, others annealed at different temperatures ranging from 600 °C to 1100 °C) is plotted in Fig. 1a. Four peaks can be observed for the sample measured at room temperature at 2θ positions 18.4 °, 37.54 °, 41.74 ° and 57.62 ° corresponding to ZGO(111), ZGO(222), Al_2O_3 (006) and ZGO(333), respectively, which can be corroborated in Refs. [23,24]. For a cubic system, the lattice parameter, a, can be calculated from the equation $a = d_{hkl}\sqrt{h^2 + k^2 + l^2}$ using interplanar spacing obtained from the Bragg's Law [25], $n\lambda = 2d_{hkl} \sin\theta$. Where a is the lattice parameter, d_{hkl} is the interplanar spacing between hkl planes, n is the order of diffraction (n = 1,2,3 …), λ is the wavelength of X-ray source, and θ is the angle of incidence. The obtained lattice parameter of the ZGO film is 8.293 Å, which is slightly smaller than the value of 8.333 Å reported from ZGO single crystal [26] or reference data for cubic ZGO (space group: $Fd\bar{3}m$, space group number: 227, $a = b = c = 8.33$ Å, and $\alpha = \beta = \gamma = 90°$, ICSD collection code: 9394). The cause was attributed to the deficiency of Zn, evidenced by x-ray photoemission spectroscopy, as the atomic radii of Zn^{2+} (0.74 Å) is larger than Ga^{3+} cations (0.63 Å) [24], which could result in the shrinkage of lattice. In the higher temperature region between 850 °C – 1100 °C, these four peaks are still presented at all annealing temperatures while the intensity drops gradually with increasing annealing temperature. However, no additional peak is obviously seen in this region, indicating that the epitaxy is kept even at very high annealing temperature up to 1100 °C.

To obtain a more granular understanding of the structural variations, a short-range $\theta/2\theta$-scan (36.5 ° to 38.5 °) and XRC measurements at ZGO (222) were performed during the same annealing period. From Fig. 1b, it can be observed that as the annealing temperature was increased from 25 °C to 600 °C, the ZGO (222) peak shifts to smaller 2θ values, from 37.54 ° to 37.36 °. This incremental shift is observed until the annealing temperature reaches 850 °C, at which point the ZGO (222) peak position stabilizes at 37.24 °. Such a peak shift to smaller 2θ values is mostly attributed to thermal expansion of interplanar spacing along out-of-plane direction, i.e., $d_{\{111\}}$. However, the lattice expansion halts at around 850 °C, as the ZGO (222) peak shift stagnates. Contrarily, as the temperature increases from 850 °C to 1100 °C, the ZGO (222) peak shifts towards higher 2θ values from 37.24 ° to 37.45 °, respectively (indicating a shrinkage of d_{222}). Meanwhile, the full width at half maximum (FWHM) of the 2θ peak broadens with increasing temperature, potentially signaling a compositional alteration or decomposition of the ZGO film. Complementary XRC measurements shown in Fig. 1c further substantiate this observation. The FWHM for ZGO (222) peak stays relatively unchanged from 25 °C to 800 °C, highlighting the material's impressive thermal resilience in an air ambience. However, from 850 °C the FWHM continues to broaden until the annealing temperature reaches 1100 °C. This suggests an increase in the degree of mosaic tilt as a consequence of the material quality degrading with temperature. This collective information is summarized in Fig. 1d: the FWHMs of 2θ and XRC of ZGO (222) peaks, as well as the corresponding interplanar spacing (d_{222}) is plotted as a function of annealing temperature (T_A [4]). We can identify three distinct regions in the diagram.

(I) *Elastic region* (T_A < 750 °C): the FWHMs of 2θ and XRC has no obvious change, while the lattice expands with T_A due to the thermal strain. This result indicates that there is no obvious structural degradation.

(II) *Plastic region* (750 °C < T_A < 850 °C): the lattice continuously expands with increasing T_A. Meanwhile, the FWHM of both 2θ and XRC broadens, implying the onset of crystal quality degradation due to the emergence of structural defects such as point defects, dislocations, and grain boundaries.

(III) *Out-diffusion region* (T_A > 850 °C): a clear transition in d_{222} spacing can be seen at 850 °C, where the lattice expansion ceases, and instead, lattice shrinkage occurs with increasing T_A. This gives a strong indication that the film's composition is changing during annealing, potentially as a result of vacancy formation or host atom substitution by smaller atoms, leading to a quaternary alloy formation. Under this circumstance, the FWHM of both 2θ and XRC further expands because of random alloying and film quality degradation.

It is noteworthy that even at the extreme temperature of 1100 °C, the material's crystal quality remains relatively intact. This is evidenced by the sharp 2θ and XRC peaks with small FWHMs of 0.35 ° and 0.71 °, respectively, demonstrating a high thermal stability. No other crystal orientation was observed, indicating the preservation of the epitaxial relationship of ZGO (or newly formed quaternary alloy) with sapphire at these elevated temperatures.

To further study the cause of peak broadening and shift during *in-situ* annealing measurement, *ex-situ* XRD measurements were performed

[4] Annealing temperature.

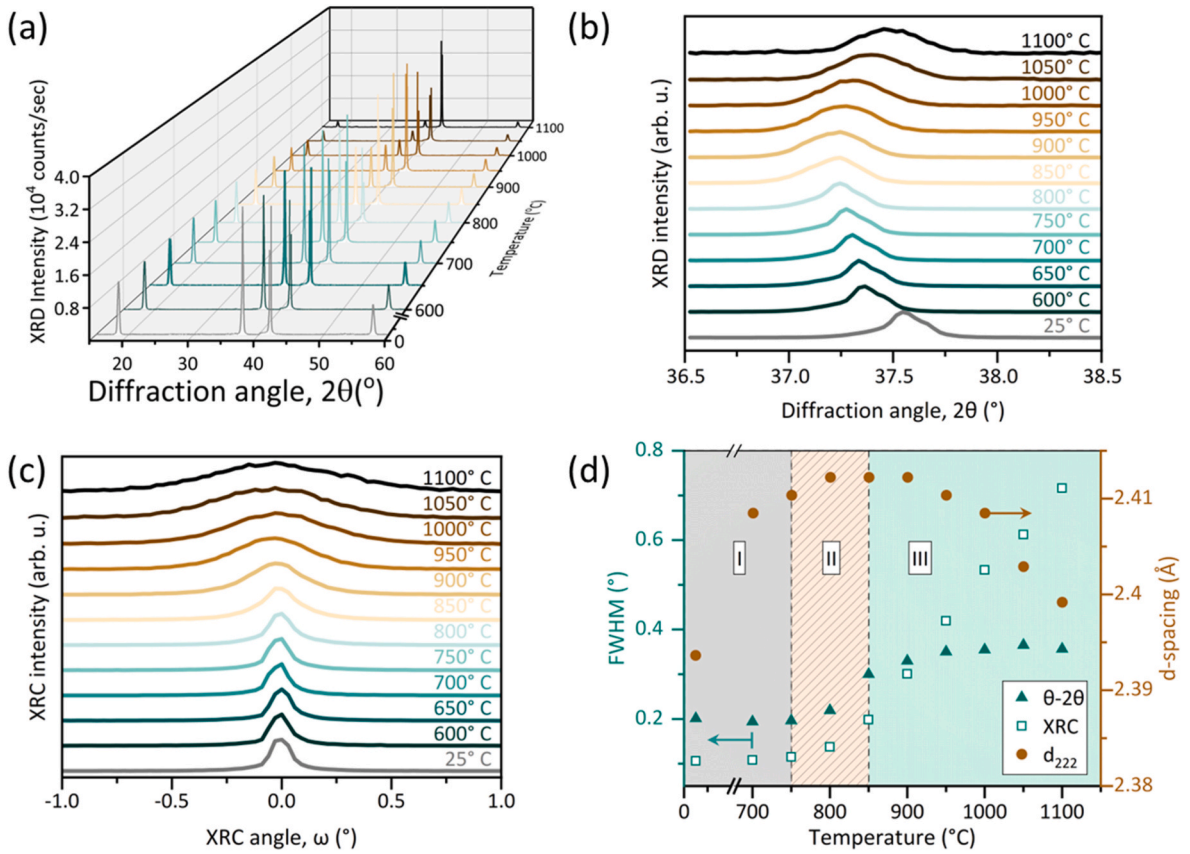

Fig. 1. In-situ XRD $\theta/2\theta$-scan measurement for different annealing temperatures. (a) a waterfall plot of long-range scans, (b) Short-range scans around ZGO (222) peak, (c) corresponding XRCs at ZGO(222), and (d) interplanar spacing (d_{222}) and FWHM of 2θ and XRC of ZGO (222) peak as a function of annealing temperature. The diagram is divided into I) Elastic, II) plastic, and III) out-diffusion regions.

after cooling down the samples from annealing temperatures to room temperature (in air ambience) to exclude the effect of thermal strain. It is worth mentioning that the samples used in these measurements were of identical quality. Up to 800 °*C*, no substantial shift or broadening was observed for the three ZGO {111} peaks as seen in $\theta/2\theta$ scans in Fig. 2a. This reinforces the high thermal stability of the material up to 800 °*C* in air. Upon further increasing the annealing temperatures to 950 °*C* and 1100 °*C*, a slight loss of intensity and a noticeable peak shift towards higher 2θ angles are observed. For instance, the ZGO (111), ZGO (222) and ZGO (333) peaks shift from 18.45 ° to 18.85 °, 37.54 ° to 38.08 °, 57.61 ° to 58.51 °, at 800 °*C* and 1100 °*C*, respectively, indicating a permanent change in composition. The corresponding XRC measurements reveal an obvious broadening of FWHM for the samples annealed at 950 °*C* and 1100 °*C*. Here, the measured FWHMs are 0.10 °, 0.11 °, 0.12 °, 0.37 °, and 0.70 °, corresponding to T_A at 25 °*C*, 750 °*C*, 800 °*C*, 950 °*C*, and 1100 °*C*, respectively, as seen in Fig. 2b. These XRC results corroborate that composition change in the film also leads to degradation of quality.

Several plausible factors could be driving the observed compositional change. As the sample was annealed in air, it is possible that ZGO

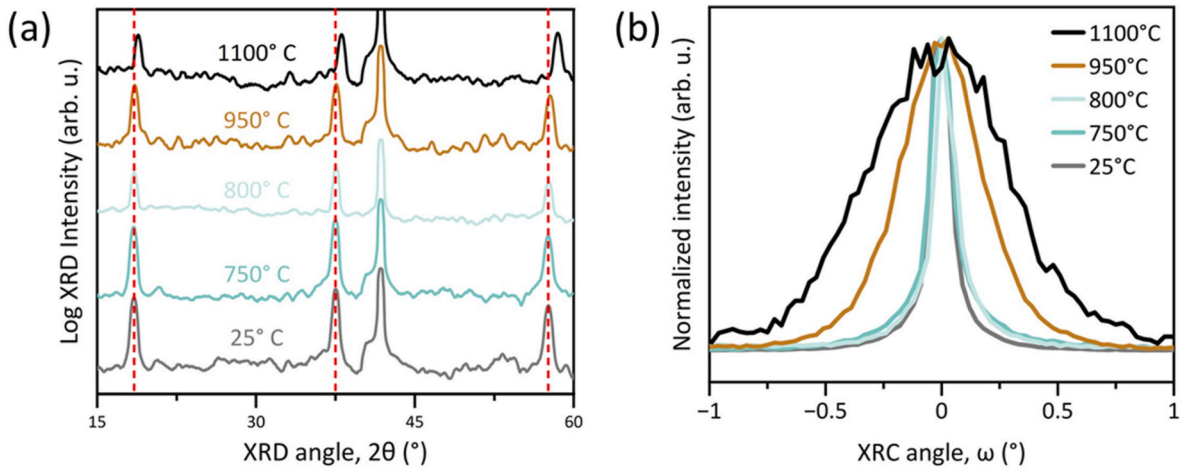

Fig. 2. Ex-situ XRD measurements. (a) Semi-logarithmic scale plots of $\theta/2\theta$ scans and (b) corresponding XRCs of ZGO (222), measured after cooling down samples from annealing to room temperature.

decomposition resulted in the formation of ZnO and $\beta-$ Ga_2O_3 due to precipitation of Zn or Ga atoms interacting with oxygen. However, no pure phase of ZnO or $\beta-Ga_2O_3$ is observed in the 2θ XRD patterns [24,27]. As Al^{3+} has a smaller radius (0.57 Å) than Ga^{3+}, the spinel structure of $ZnAl_2O_4$ (space group: $Fd\bar{3}m$, space group number: 227, $a=b=c=$ 8.086 Å, and $\alpha=\beta=\gamma=90°$, ICSD collection code: 26849) has smaller lattice parameter than ZGO, which results in the peak shift towards higher 2θ angles. It is also worth considering the formation of quaternary alloy, $Zn(Al_xGa_{1-x})_2O_4$ (ZAGO), being driven by the interdiffusion between ZGO and sapphire. Other possibilities, such as the formation of high Zn-deficient ZGO or phase transformation of β - Ga_2O_3 with doped Zn, should not be entirely ruled out.

3.2. Microstructural analyses of ZGO thin films before and after annealing

To resolve the change of composition after high temperature annealing, as-grown and 1100 °C annealed samples were further characterized by HRTEM and EDS. Fig. 3a shows a TEM bright-field cross-sectional image of an as-grown ZGO epitaxial thin film with a thickness of about 101 nm on sapphire substrate. There are strain fields visible in the epitaxial ZGO thin film close to the interface region, which can result from a large lattice mismatch [24]. No obvious grain boundary and threading dislocation are presented in the film. The epitaxial relationship between ZGO and sapphire substrate is indexed as an in-plane epitaxial relationship along $[110]_{ZnGa_2O_4}//[120]_{Al_2O_3}$ and the $(\bar{1}1\bar{1})$ of ZGO is parallel to the (003) of sapphire substrate in the selected area electron diffraction (SAED) pattern in Fig. 3b. The crystal structure of ZGO was identified as cubic and the lattice parameters were calculated as $a=b=c=8.28$ Å, and $\alpha=\beta=\gamma=90°$, which agrees with XRD result and reference data for cubic ZGO. Here, the lattice parameter of ZGO is calibrated using strain-free *c*-lattice constant of sapphire, 12.98 Å. The thin films were composed of ≈22.1 at. % Ga, 68.3 at. % O, 1.5 at. % Al, and 8.1 at. % Zn as can be observed from the EDS line scan of Fig. 3c. The result shows that the film might be grown slightly deficiency in Zn because of a low Zn/Ga ratio ≈0.36, which explains why the lattice constant is smaller than reported value measured from bulk ZGO [26]. A HRTEM image taken at the interface between the ZGO thin film and sapphire is displayed in Fig. 3d. The lattice distortion marked with an arrow at the interface between ZGO and sapphire is due to their lattice mismatch. The epitaxial {111} ZGO thin films grown on {001} sapphire substrates using MOCVD have been studied earlier [1,28,29]. It was observed that the apparent strain is released as the thickness increases and is caused due to misfit dislocations. The Fast Fourier Transform (FFT) diffraction patterns taken from the bottom and up regions of the HRTEM image are corresponding to sapphire with [120] zone axis and ZGO with [110], respectively, shown in Fig. 3e and f. No secondary phase can be distinguished in the ZGO pattern, further evidence that the ZGO was grown in single phase and epitaxially on sapphire at early nucleation stage.

Fig. 4a shows a TEM bright-field cross-sectional image of ZGO and sapphire after thermal annealing at 1100 °C. It can be observed that an intermediate layer has been formed at the interface between the original ZGO layer and the sapphire substrate. The interface between the newly formed intermediate layer and the substrate remains smooth, while the interface between the top and intermediate layer is much rougher. In addition, some grain boundaries can be seen in the top layer. The thicknesses of the two layers were measured to be ≈ 100.3 and 50.3 nm, respectively. Compared to as-grown ZGO thin film, see Fig. 3a, the thickness of the top ZGO layer did not change significantly after a thermal annealing of 1100 °C. However, the EDS line scan (Fig. 4b) shows that about 12 at. % of Al have diffused from sapphire into the top layer to form a quaternary ZAGO (marked as $Zn(Ga,Al)_2O_4$ in figure) alloy. Where, this top ZAGO layer is found to be composed of ≈8.8 at. % Zn, 12.0 at. % Ga, 12.6 at. % Al, and 66.6 at. % O. The Zn and O concentrations have no big difference to the as-grown ZGO film, while the Ga concentration drops owing to the incorporation of out-diffused Al from sapphire. In addition, the Ga from the ZGO have out-diffused into the sapphire to form a new β-AGO (marked as $(Ga,Al)_2O_3$ in figure) layer at the interface, and its composition is found to be ≈ 20.0 at. % Ga, 9.3 at. % Al, and 70.7 at. % O. Fig. 4c shows SAED of the annealed sample. With unravelling the pattern, three crystal structures are found and referred to ZAGO, AGO, and sapphire. The crystal structure of ZAGO was identified and calculated to be cubic with $a=b=c=8.22$ Å, and α = β = γ = 90 °, which is in in good correspondence with spinel ZGO structure but has a smaller lattice parameter. If the interdiffusion results in only Ga atoms in host lattice substituted by diffused Al atoms, the relative concentration of Al, x, in spinel $Zn(Al_xGa_{1-x})_2O_4$ calculated from Vegard's law is around 0.45. (Note: calculated concentration can be different depending on the use of reference data for ZAO lattice parameter.) This matches well with the x value, around 0.5, determined by EDS. The result indicates that the spinel ZAGO system has a wide range of miscibility. The crystal structure of AGO was identified as monoclinic and the lattice parameters were calculated as $a=11.84$ Å, $b=2.98$ Å, $c=5.77$ Å, and $\alpha=\gamma=90°$, $\beta=103°$, which is in good correspondence with the β–Ga_2O_3 (monoclinic, space group: *C2/m* (No. 12), $a=12.21$ Å, $b=3.04$ Å, $c=5.80$ Å, and $\alpha=\gamma=90°$, $\beta=103.83°$, ICSD collection code: 83645). In addition, the layers are formed epitaxially to the sapphire substrate with zone axes of $[110]_{Zn(Ga,Al)_2O_4}//[0\bar{1}0]_{(Ga,Al)_2O_3}//[120]_{Al_2O_3}$ and the epitaxial habit plane of $(\bar{1}1\bar{1})_{Zn(Ga,Al)_2O_4}//(20\bar{1})_{(Ga,Al)_2O_3}//(003)_{Al_2O_3}$. Fig. 4d shows HRTEM images of AGO and sapphire substrate, indicating that this intermediate film grows along with the [001] of the sapphire substrate. The corresponding FFT diffraction patterns with zone axes of sapphire and AGO along with [120] and [010] are shown in Fig. 4e and f, respectively, and the $(\bar{2}01)$ of AGO is parallel to (003) of sapphire. This is consistent with results by Shinji and Yoshihiro [30], indicating that the $(\bar{2}01)$ plane of β–Ga_2O_3 grows parallel to the (001) plane of sapphire. Fig. 4g shows a HRTEM image taken at interface of ZAGO and AGO layers. The corresponding FFT diffraction patterns of $\beta-(Ga,Al)_2O_3$ with [010] zone axis and $Zn(Ga,Al)_2O_4$ with [110] zone axes are shown in Fig. 4h and i, respectively. The epitaxial habit plane is identified as $(\bar{1}1\bar{1})$ of $Zn(Ga,Al)_2O_4$ and $(20\bar{1})$ of $\beta-(Ga,Al)_2O_3$.

3.3. Formation mechanism of ZAGO and AGO based on density functional theory (DFT)

A possible mechanism for the formation pathways of ZAGO and AGO is rationalized through processes involving diffusion and restructuring. To support the formation pathways for ZAGO and AGO described above, the compounds of interest were geometrically optimized/relaxed at the PBE level of theory of DFT/GGA and their formation energies (as compared to the chemical potentials of the corresponding pure metals and O_2 gas) were obtained according to: 2.18 eV/at ($ZnGa_2O_4$), −3.02 eV/at ($ZnAl_2O_4$), −2.8 eV/at ($\beta-$ AlGaO$_3$), −2.27 eV/at ($\beta-$ Ga_2O_3), and −3.43 eV/at (sapphire: Al_2O_3), respectively.

The substitution cost for an Al atom (at an empty Ga site) in ZGO thus transforming it into ZAGO was evaluated to be 0.74 eV, while the substitution cost for a second Al atom (i.e., after one Al atom is already incorporated in the $ZnGa_2O_4$ supercell) decreases to 0.59 eV. The substitution cost for an Al atom (at an empty Ga site) in $\beta-Ga_2O_3$ thus transforming it into AGO was evaluated to be 0.51 eV, while the substitution cost for a second Al atom (i.e., after one Al atom is already incorporated in the $\beta-Ga_2O_3$ supercell) remains nearly the same at 0.48 eV. The substitution cost for a Ga atom (at an empty Al site) in sapphire was evaluated to be 0.14 eV, while the substitution cost for a second Ga atom (i.e., after one Ga atom is already incorporated in the sapphire supercell) decreases to 0.12 eV. These substitution costs are summarized in Table 1. In these evaluations of the substitution costs, all

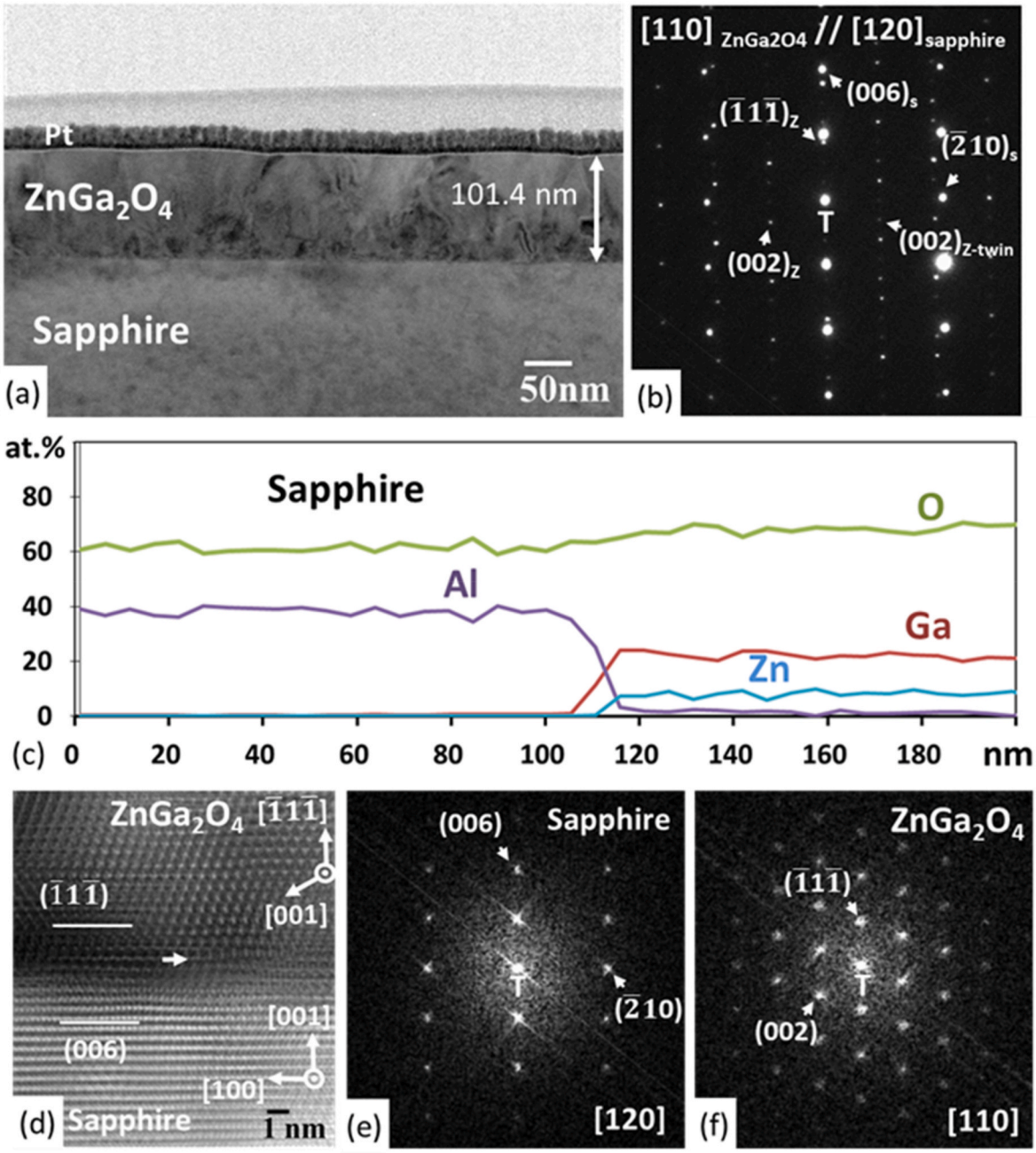

Fig. 3. (a) Cross-sectional TEM image and (b) SAED of $ZnGa_2O_4$ and sapphire with zone axes of $[110]_{ZnGa_2O_4}//[120]_{Al_2O_3}$, (c) EDS line scan of $ZnGa_2O_4$ and sapphire, (d) HRTEM image of $ZnGa_2O_4$ and sapphire along with the zone directions of Fig. 3b; FFT diffraction pattern of (e) sapphire with zone axis [120] and (f) $ZnGa_2O_4$ with zone axis of [110].

possible substitution sites have been investigated; thus, the mentioned substitution costs should be perceived as minimum values.

These modelling results indicate that substitution of Ga atoms in sapphire is energetically much cheaper, this is why we identify the out-diffusion of Ga as being the main driving force behind the interdiffusion process. This could be corroborated from the EDS line scan in Fig. 4b where we see higher at. % of Ga present in AGO compared to ZAGO (20 at. % in AGO compared to 12 at. % in ZAGO). It is also predicted from the DFT modeling that Al diffusion is easier when initial quantities of Al are already present in a system. This is possibly why the meta-stable defective film evolves into stable β - phase AGO. The substitution costs should be seen in the perspective of the thermal energies at temperatures relevant to the deposition and annealing processes of these materials. The thermal energies for Ga occupying an Al site in sapphire can be estimated to be $\approx$ 0.100 eV at 850 °C and $\approx$0.122 eV at 1100 °C. Based on this relatively small difference in thermal energies at 850 °C and 1100 °C, the values of the formation energies and substitution costs as obtained from DFT simulations, and also based at the discussions in section 3.1, we identify the threshold temperature for interdiffusion and formation of ZAGO and AGO to be about 900 °C.

The formation mechanism of ZAGO and AGO is sketched in Fig. 5 and could be qualitatively described according to Eq. (3).

$$2Ga + Al_2O_3 \rightarrow Ga_2O_3 + 2Al \quad (3)$$

Upon reaching a threshold temperature (i.e., acquiring sufficient thermal energy), Ga atoms leave their respective sites in spinel ZGO and diffuse towards the sapphire substrate (Fig. 5a). Here, Ga diffuses through the Al vacancies of the substrate and prompts the formation of a

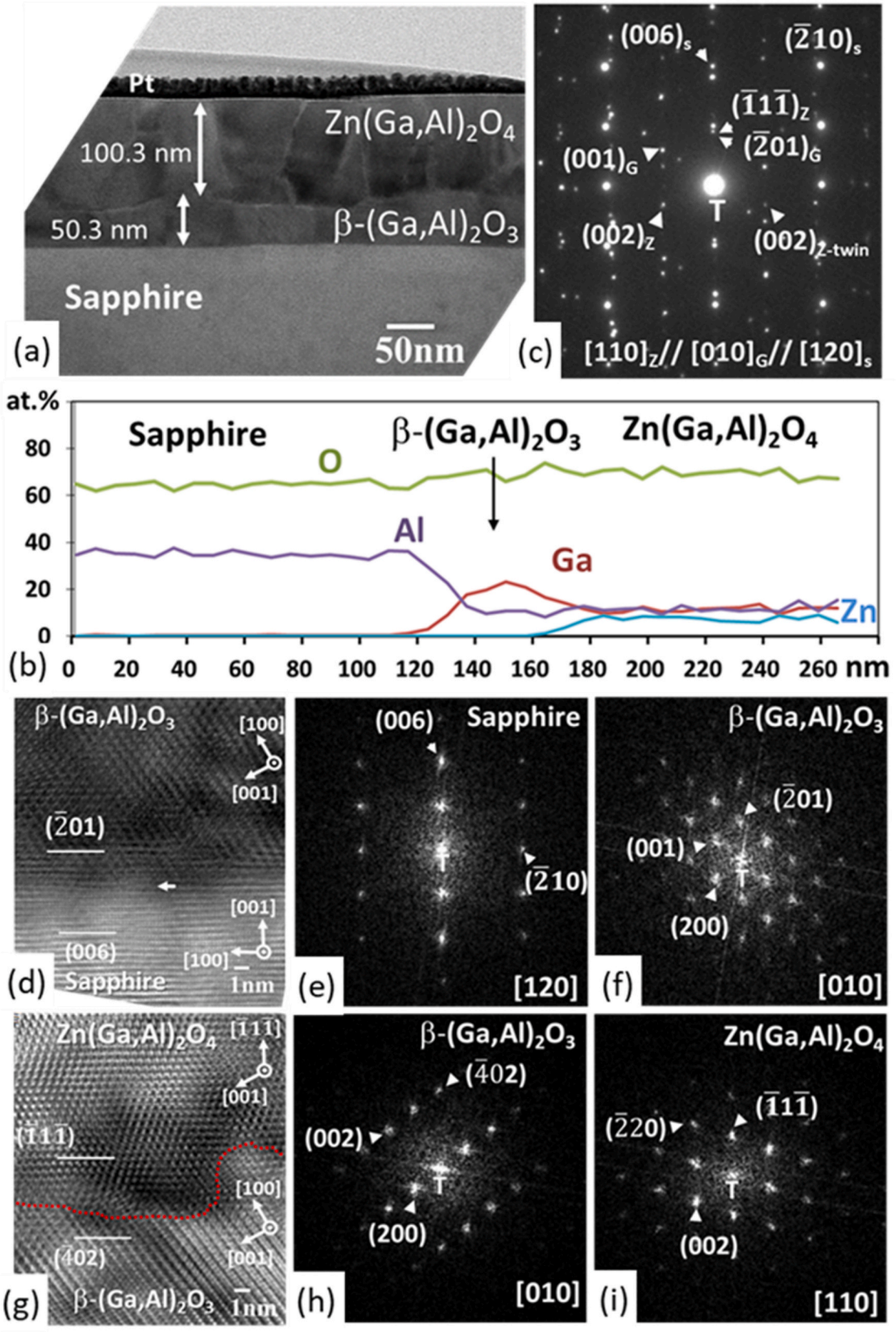

Fig. 4. (a) Cross-sectional TEM image and (b) EDS line scan of the $ZnGa_2O_4$ and sapphire after thermal annealing at 1100 °C, (c) SAED of $Zn(Ga,Al)_2O_4$, β–$(Ga,Al)_2O_3$, and sapphire with zone axes of $[110]_{Zn(Ga,Al)_2O_4}//[010]_{\beta-(Ga,Al)_2O_3}//[120]_{Al_2O_3}$, (d) HRTEM image of $\beta-(Ga,Al)_2O_3$ and sapphire along with the zone directions of Fig. 3c; FFT diffraction pattern I(e) sapphire with zone axis of [120] and (f) $\beta-(Ga,Al)_2O_3$ with zone axis of [010], (g) HRTEM image of $Zn(Ga,Al)_2O_4$ and $\beta-(Ga,Al)_2O_3$ along with the zone directions of Fig. 3c; FFT diffraction pattern of (h) $\beta-(Ga,Al)_2O_3$ with zone axis of [010] and (i) $Zn(Ga,Al)_2O_4$ with zone axis of [110].

Table 1
Summary of substitution costs of Al in ZGO and GAO, as well as Ga in sapphire.

Substitution costs	Al in ZGO (eV)	Al in GAO (eV)	Ga in sapphire (eV)
1st atom	0.74	0.51	0.14
2nd atom	0.59	0.48	0.12

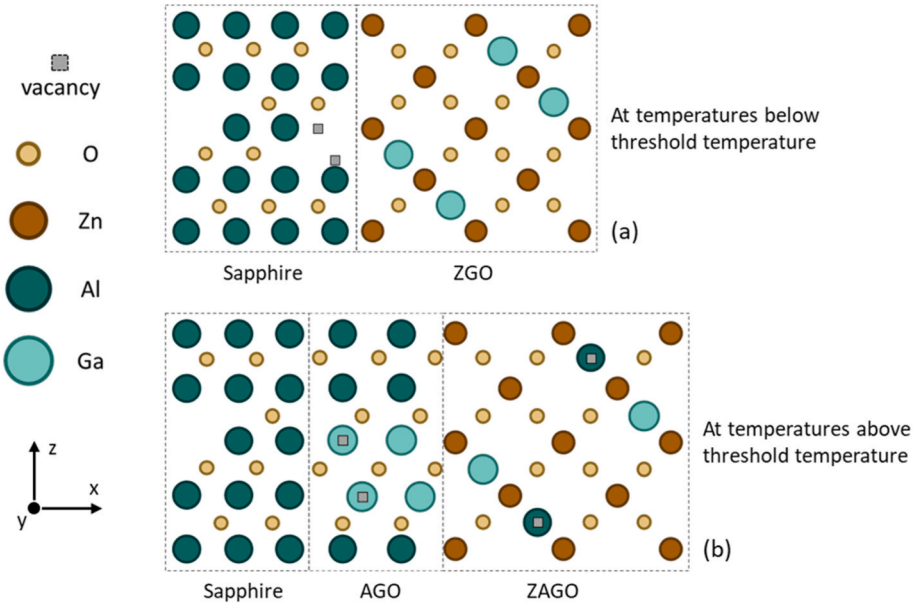

Fig. 5. Schematic projection of the formation mechanism of AGO and ZAGO illustrating the structural evolution of materials in the x-z plane (a) below and (b) above the threshold temperature.

meta-stable defect-rich film at the interface, which later evolves into the (energetically more favorable) β - AGO. Formation of the intermediate defect film coupled with the high annealing temperature provides the necessary threshold thermal energy for further out-diffusion of Al atoms from the substrate. After the evolution of the defect-rich film into β - AGO, further incorporation of Al is suppressed due to the considerable thermodynamic stability of the β - phase. This situation results in further transport of Al to the ZGO thin film. Here, the presence of Ga vacancies lowers the formation energy threshold to allow for the interdiffusion and results in the formation of quaternary ZAGO (Fig. 5b).

3.4. Optical properties of as-grown and thermal annealed ZAGO and AGO thin films

The optical properties such as refractive index (n), extinction coefficient (k) and absorption coefficient (α) of the samples were determined using Mueller Matrix Spectroscopic Ellipsometry (MMSE[5]) by fitting an optical model to the experimental data. The direct and indirect optical bandgap energies (E_g) were then determined by the linear extrapolation of α using *modified Cody formalism* [31,32] according to the methodology in Ref. [33] to investigate if quaternary ZAGO retained the high E_g values as ZGO. Fig. 6a and b describe the optical model established for analysis of the measured ellipsometric data for as-grown and annealed samples, respectively. The optical model established for as-grown samples in our previous work [33] consisted of a semi-infinite sapphire substrate, the ZGO thin film, a roughness layer and air (void) as the ambient. In this work, this model has been updated to account for the thermally induced β –AGO intermediate layer as shown in Fig. 6b, to extract its intrinsic optical properties.

The optical constants of a bare sapphire substrate with an unpolished backside were obtained using a Tauc-Lorentz (TL[6]) oscillator model. The effective optical properties of both ZAGO and AGO are described using a Herzinger–Johs (HJ[7]) parameterized semiconductor (PSemi) oscillator function-based model [33–35]. The overlayer employed to represent surface roughness in the samples was modelled as a 50/50 mixture of ZAGO and ambient (air) using a Bruggeman Effective Medium Approximation [36,37], with thickness as the only regression parameter. Surface roughness (d_r), thickness of ZAGO (d_1) and AGO (d_2), and optical properties of the films were then determined by fitting the optical model to the experimental data. A Levenberg-Marquardt multivariate regression algorithm was used to minimize the mean squared error (MSE[8]) between the measured and modelled data [38,39].

The different samples used in this study are described along with their process parameters and calculated values in Table 2. The shape parameters of the HJ oscillator were fixed while amplitude, broadening and central energy parameters of the oscillator were allowed to vary. A good fit (MSE = 1.9) was obtained between the modelled and experimental data for as-grown sample 1a and its thickness, roughness and optical constants were obtained by regression analysis. The resulting optical constants of sample 1a were found to be identical to our previous results [33] and to the results reported by Hilfiker et al. for single crystalline bulk-like ZGO [40]. In contrast, the annealed samples (1b – 1d) resulted in a comparatively higher MSE and the features in the ψ and Δ spectra were observed to shift towards lower E as the annealing temperature was increased. In Fig. 7, an additional interference fringe can be observed for sample 1d compared to samples 1(a-c) along with an overall denser distribution of the fringes, suggesting an increase in the total film thickness.

From the analysis of the annealed samples and guided by the XRD and TEM results in section 3 (3.1 and 3.2), an additional layer was introduced to represent AGO. ZAGO was represented using the initial HJ oscillator but with varying amplitude, broadening and central energy parameters to account for changes in its dielectric function (ε_{ZAGO}) due to diffusion of Al. The added layer representing AGO was initially

[5] Mueller matrix spectroscopic ellipsometry.

[6] Tauc-Lorentz.

[7] Herzinger-Johs.

[8] Mean squared error.

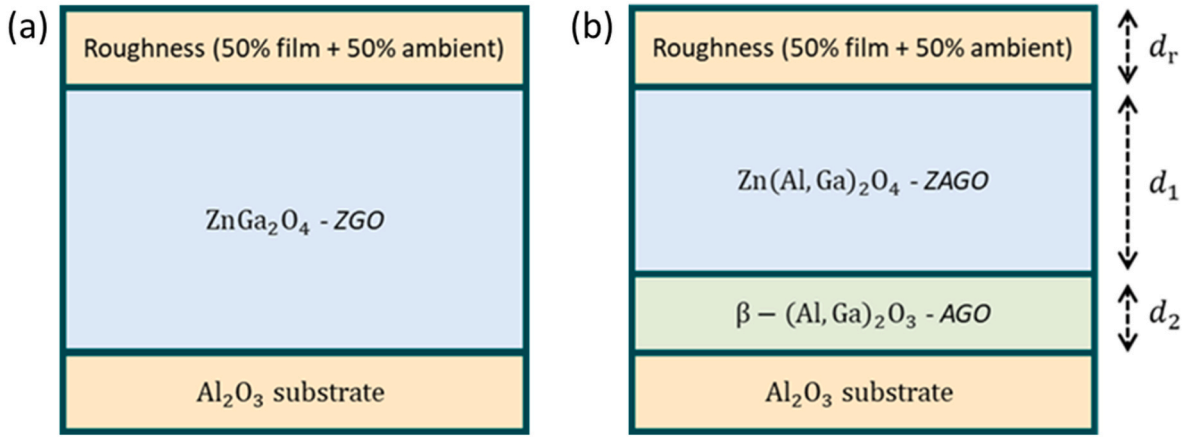

Fig. 6. Optical model description of (a) as-grown and (b) annealed samples, with 'd' representing thickness of respective layers.

Table 2
Summary of different parameters for room temperature and annealed samples.

Sample	Annealing temperature (°C)	d_r (nm)	d_1 (nm)	d_2 (nm)	ZAGO direct E_g (eV)	ZAGO indirect E_g (eV)
1a	–	1.36 ± 0.00	105.07 ± 0.01	–	5.06 ± 0.01	4.70 ± 0.01
1b	800 °	0.91 ± 0.00	105.87 ± 0.01	–	5.07 ± 0.02	4.75 ± 0.01
1c	950 °	1.52 ± 0.00	103.7 ± 2.13	13.83 ± 0.03	5.20 ± 0.00	4.85 ± 0.01
1d	1100 °	1.99 ± 0.01	98.98 ± 0.24	48.99 ± 0.24	5.72 ± 0.02	5.45 ± 0.00

implemented using a Cauchy dispersion model in the transparent region of the film ($\geq$ 310 nm or $\leq$ 4 eV) according to Eq. (4),

$$n(\lambda) = A + \frac{B}{\lambda^2} + \frac{C}{\lambda^4} \tag{4}$$

where, n is the refractive index, A, B and C are fitting parameters and λ is the wavelength. This model estimated d_2 and a polarization averaged isotropic dielectric function [41,42] $\varepsilon_{AGO} = n^2$. Keeping these initial estimates, the Cauchy model was then transformed into another HJ oscillator model, to account for ε_{AGO} across the full spectral region (0.7–5.9 eV) of the ellipsometer. The amplitude, broadening and central energy parameters of the HJ oscillator were allowed to vary, while the shape parameters and d_2 (obtained from Cauchy dispersion earlier) were kept fixed. It should be noted that $\beta-$AGO has a monoclinic structure, which means AGO should exhibit anisotropic optical properties along its different crystallographic axes. However, the formation of this film was unintentional, and its growth parameters were not optimized to achieve the highest crystal quality. Moreover, our investigation of the measured Mueller matrix data of the sample (provided in the Supplementary document, Fig. S1) did not reveal any anisotropic response. We suspect the interstitial position of the film, its small thickness, and its sub-optimal crystal quality made it less sensitive for the detection of its individual anisotropic tensor components using MMSE. Therefore, the analysis of anisotropy of AGO is out of the scope of this paper. Optical details on high-quality AGO can be found elsewhere [41].

Subsequently, all three annealed samples were analyzed with the updated optical model and a good fit (MSE $\approx$ 2) was obtained between modelled and experimental data, with no significant correlation between the fit parameters (model fit to the experimental data is shown in Fig. 7). The resulting d_r, d_1 and d_2 values for the three samples are summarized in Table 2.

From Tables 2 and it is observed that samples 1a and 1b show no presence of an intermediate layer while samples 1c and 1d show the AGO film presence between ZAGO and substrate. Also, from XRD and XRC measurements in Fig. 1, no significant change in the FWHM of $\theta/2\theta$ peak for ZAGO can be observed up to 800 °C. This suggests that annealing temperatures in the range of 800–900 °C could be regarded as

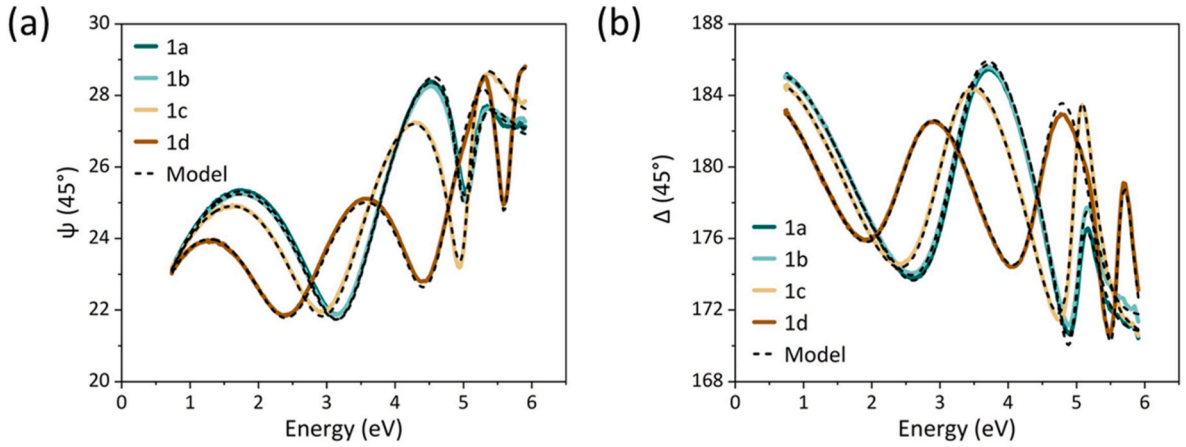

Fig. 7. Experimental & model data of (a) ψ and (b) Δ spectra at 45 ° angle of incidence (AOI) for samples 1(a–d).

the threshold for the formation of β - AGO. The AGO thickness at 850 °C was found to increase slightly (≈0.8 nm) but a clear image confirming its presence at the interface could not be obtained and corroborated using TEM. As annealing temperatures are increased, d_2 increases to 13.83 nm and 48.99 nm for sample 1c and 1d, respectively. d_2 for sample 1d was corroborated using TEM and was found to be in excellent agreement with that observed using SE (Figs. 3 and 4 for samples 1a and 1d, respectively). Increasing the annealing temperature resulted in shifting of the optical constants, n, k, and α, spectra to higher energies for ZAGO, as shown in Fig. 8. The optical constants of AGO are observed to be slightly smaller than those of the ZAGO film, as shown in Fig. 9 (It is to be noted that these are presented as isotropic averages of its anisotropic dielectric tensor). These optical constants are observed to match well with the optical constants in the extraordinary direction (ε_{zz}) as obtained by Hilfiker et al. for pure phase $\beta-$ AGO grown on (010) oriented $\beta-Ga_2O_3$ [41].

The line-shape of α for ZAGO was then analyzed according to the *modified Cody formalism* to determine its direct and indirect E_g. Comparing samples 1a and 1c, an increase in direct E_g of about 0.14 eV was observed, along with an increase of approximately 12.46 nm in total film thickness. This corroborates that inter-diffusion between thin film and substrate and formation of AGO possibly begins at about 900 °C. Further increase in annealing temperature results in further shifting of E_g to 5.72 eV as can be observed in sample 1d. This increase in E_g is attributed to the high diffusion of Al at higher temperatures leading to the formation of wider E_g quaternary material, which can be confirmed from the EDS line scans in Fig. 4c where the relative concentration x in $Zn(Al_xGa_{1-x})_2O_4$ is around 0.5 in sample 1d. This process potentially disrupts the crystal lattice, creating local variations in the electronic environment by altering the bonding characteristics, which in turn leads to changes in the band structure. Although no reports for the E_g of ZAGO could be found in literature, several studies have reported a similar trend of increase in E_g due to incorporation of Al [20,43]. The values reported in this study are summarized in Table 2 and the linear extrapolations according to the *modified Cody formalism* are presented in Fig. 10a and b for Direct E_g and Indirect E_g, respectively. Spectral broadening in optical constants spectra (Fig. 8) and in the absorption tail of ZAGO in the annealed samples was however observed to be minimal. This corroborates that while Al diffusion does affect the optical properties, the overall crystal quality does not degrade significantly.

4. Conclusion

We have studied the thermal stability of high-quality ZGO epifilms on sapphire substrates and the formation of quaternary ZAGO epilayer using *in-situ* annealing XRD and XRC measurements ranging in temperatures from 600 to 1100 °C in air. The ZGO epifilm exhibited and maintained excellent crystal quality without degradation even at high temperatures up to 750 °C. This was confirmed by a narrow XRC peak with a small FWHM value of 0.1 °. Further increase in annealing temperature to 850 °C resulted in slight degradation in quality, and incorporation of Al into the ZGO film took place at even higher temperatures. The formation of an epitaxial ZAGO layer, coupled with an intermediate epitaxial β - AGO layer between ZAGO and the sapphire substrate, was confirmed via *ex-situ* XRD, TEM, EDS, and SE measurements. In addition, our analysis revealed that the incorporation of Al in the ZGO layer amplified with higher annealing temperatures. TEM-EDS measurements revealed that the Zn content in ZGO layer remained unchanged before and after annealing, while the Ga content decreased, and the Al content increased. Meanwhile, the ZAGO layer retained its cubic spinel structure with high quality. Consequently, we hypothesize that the formation of quaternary ZAGO is driven by interdiffusion between the ZGO thin film and sapphire substrate. The mechanism based on out-diffusion of Ga and Al from ZGO and sapphire, respectively, was corroborated by DFT evaluation of the crystalline compounds involved and their corresponding energy costs of substitution in sapphire and ZGO compounds. The thickness and optical constants of ZGO and ZAGO were determined using SE, and a line shape analysis using *modified Cody formalism* was implemented to determine its direct and indirect E_g. A shift of E_g to higher energies and a lowering of the refractive index was observed for ZAGO, which is attributed to the formation of AGO film and interdiffusion of Al from the substrate. This research, therefore, illuminates a promising pathway to engineer optical and electrical properties within the quaternary ZAGO compound system for advanced electronic devices that require high performance and reliability.

Credit author statement

Conceptualization: S.B., J.C.-C., R.-H.H., K.J., and C.-L.H.; methodology: S.B., J.-C.C., F.-G.F., W.-Y.W, E.F.A.J., G.K.G, K.-L.L, S.-H.H, J.-M.S., R.-H.H., K.J., and C.-L.H.; resources: G.K.G., R.-H.H., J.B., K.J., and C.-L.H.; data curation: S.B., J.C.-C. W.-Y.W., E.F.A.J., G.K.G, K.-L.L, S.-H.H, J.-M.S.; writing—original draft preparation: S.B., W.-Y.W., R.-H.H., and C.-L.H.; writing—review and editing: C.-L.H., G.K.G., R.-H.H., R.M., and K.J.; project administration: C.-L.H., R.-H.H. and K.J.; funding acquisition: J.B., R.-H.H., K.J, and C.-L.H. All authors have contributed to the writing and agreed to the published version of the manuscript.

Funding information

This research was funded by Vetenskapsrådet (2018–04198), Energimyndigheten (46658-1), and Stiftelsen Olle Engkvist Byggmästare (197–0210), STINT (MG2019-8485), and Stiftelsen för Strategisk Forskning (2009-00971). The Swedish Government Strategic Research Area

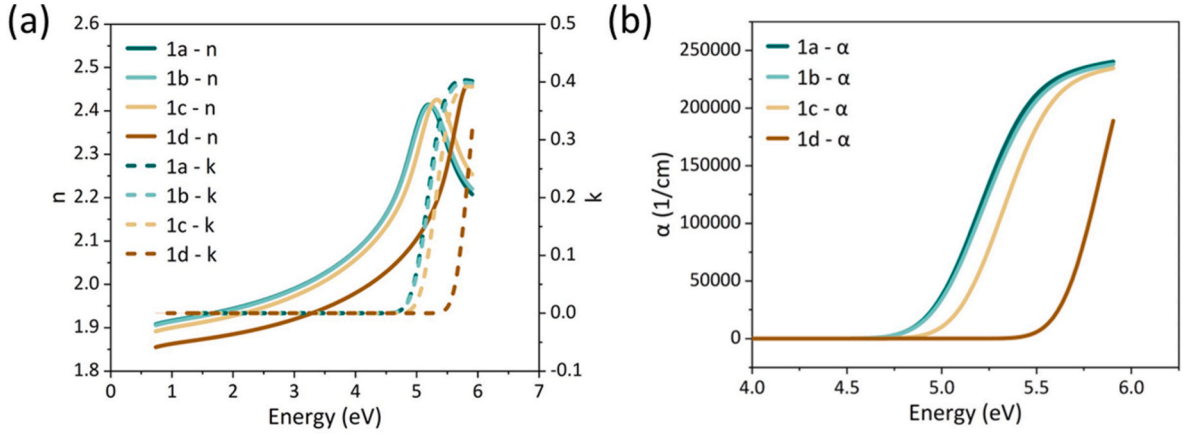

Fig. 8. (a) Optical constants and (b) absorption coefficient of ZGO and ZAGO from samples 1(a–d).

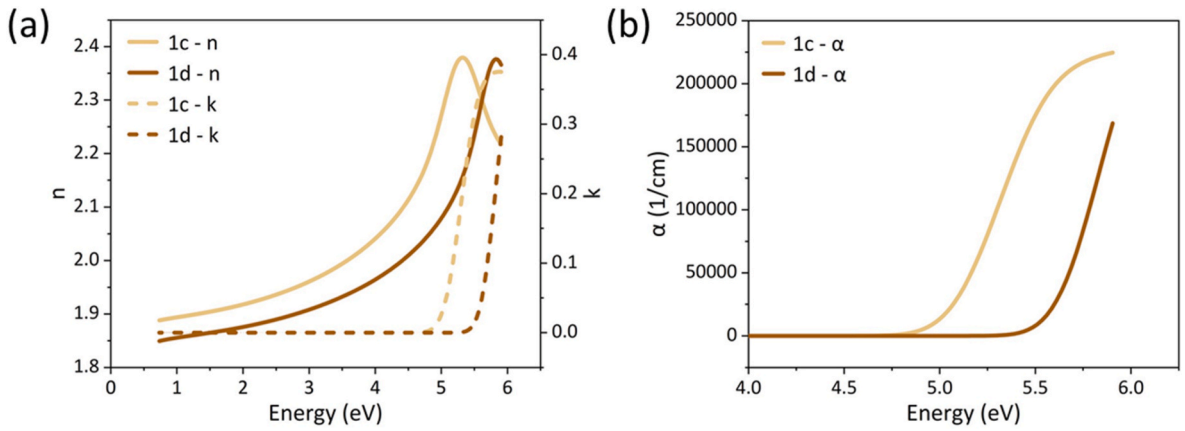

Fig. 9. (a) Optical constants and (b) absorption coefficient of AGO from samples 1c and 1d.

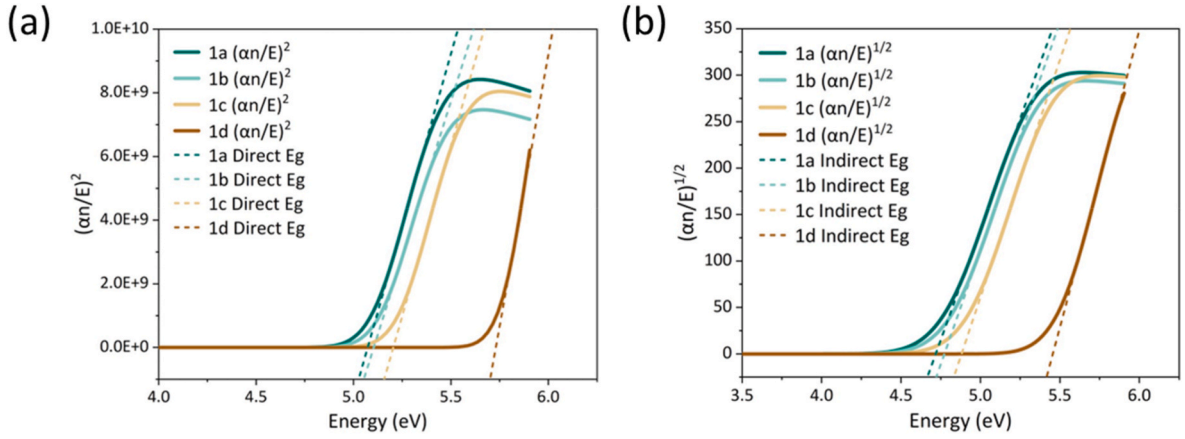

Fig. 10. (a) Direct and (b) Indirect E_g of ZAGO for samples 1 (a–d).

in Materials Science on Functional Materials at Linköping University (Faculty Grant SFO-Mat-LiU 2009-00971) is acknowledged for financial support. We acknowledge the support from Wafer Works Corporation, National Science and Technology Council (Taiwan) (112-2218-E-A49-024-MBK, 112-2622-8-A49-013-SB, MOST 111-2923-E-A49 -003 -MY3), and MAtek (2021-T-006).

Declaration of competing interest

The authors declare that they have no known competing financial interests or personal relationships that could have appeared to influence the work reported in this paper.

Data availability

Data will be made available on request.

Appendix A. Supplementary data

Supplementary data to this article can be found online at https://doi.org/10.1016/j.mtadv.2023.100422.

References

[1] R.H. Horng, C.Y. Huang, S.L. Ou, T.K. Juang, P.L. Liu, Epitaxial growth of ZnGa2O4: a new, deep ultraviolet semiconductor candidate, Cryst. Growth Des. 17 (2017) 6071–6078, https://doi.org/10.1021/acs.cgd.7b01159.

[2] S.H. Tsai, S. Basu, C.Y. Huang, L.C. Hsu, Y.G. Lin, R.H. Horng, Deep-ultraviolet photodetectors based on epitaxial ZnGa2O4 thin films, Sci. Rep. (2018) 1–9, https://doi.org/10.1038/s41598-018-32412-3, 2018 81. 8.

[3] C.H. Liao, K.H. Li, C.G. Torres-Castanedo, G. Zhang, X. Li, Wide range tunable bandgap and composition β -phase (AlGa)2O3thin film by thermal annealing, Appl. Phys. Lett. 118 (2021), https://doi.org/10.1063/5.0027067.

[4] M. Higashiwaki, K. Sasaki, H. Murakami, Y. Kumagai, A. Koukitu, A. Kuramata, T. Masui, S. Yamakoshi, Recent progress in Ga2O3 power devices, Semicond. Sci. Technol. 31 (2016), 034001, https://doi.org/10.1088/0268-1242/31/3/034001.

[5] C. Xie, X.-T. Lu, X.-W. Tong, Z.-X. Zhang, F.-X. Liang, L. Liang, L.-B. Luo, Y.-C. Wu, C. Xie, X.-T. Lu, X.-W. Tong, Z.-X. Zhang, L.-B. Luo, F.-X. Liang, L. Liang, Y.-C. Wu, Recent progress in solar-blind deep-ultraviolet photodetectors based on inorganic ultrawide bandgap semiconductors, Adv. Funct. Mater. 29 (2019), 1806006, https://doi.org/10.1002/ADFM.201806006.

[6] G.T. Dang, T. Yasuoka, Y. Tagashira, T. Tadokoro, W. Theiss, T. Kawaharamura, Bandgap engineering of α-(AlxGa1-x)2O3 by a mist chemical vapor deposition two-chamber system and verification of Vegard's Law, Appl. Phys. Lett. 113 (2018) 2–7, https://doi.org/10.1063/1.5037678.

[7] A. Hassa, H. von Wenckstern, L. Vines, M. Grundmann, Influence of oxygen pressure on growth of Si-doped β-(Al x Ga 1 − x) 2 O 3 thin films on c-sapphire substrates by pulsed laser deposition, ECS J. Solid State Sci. Technol. 8 (2019) Q3217–Q3220, https://doi.org/10.1149/2.0411907jss.

[8] W. Hu, S. Li, Y. Hu, L. Wan, S. Jiao, W. Hu, D.N. Talwar, Z.C. Feng, T. Li, J. Xu, L. Wei, W. Guo, Optical and electronic properties of (AlxGa1−x)2O3/Al2O3 (x>0.4) films grown by magnetron sputtering, J. Alloys Compd. 864 (2021) 1–9, https://doi.org/10.1016/j.jallcom.2021.158765.

[9] E. Ahmadi, O.S. Koksaldi, X. Zheng, T. Mates, Y. Oshima, U.K. Mishra, J.S. Speck, Demonstration of β-(AlxGa1-x)2O3/β-Ga2O3 modulation doped field-effect transistors with Ge as dopant grown via plasma-assisted molecular beam epitaxy, APEX 10 (2017), 071101, https://doi.org/10.7567/APEX.10.071101/AMPDF.

[10] Y. Oshima, E. Ahmadi, S.C. Badescu, F. Wu, J.S. Speck, Composition determination of β-(AlxGa1-x)2O3 layers coherently grown on (010) β-Ga2O3 substrates by high-resolution X-ray diffraction, APEX 9 (2016), 061102, https://doi.org/10.7567/APEX.9.061102/XML.

[11] A.F.M. Anhar Uddin Bhuiyan, Z. Feng, J.M. Johnson, Z. Chen, H.L. Huang, J. Hwang, H. Zhao, MOCVD epitaxy of β-(AlxGa1−x)2O3 thin films on (010) Ga2O3 substrates and N-type doping, Appl. Phys. Lett. 115 (2019), 120602, https://doi.org/10.1063/1.5123495.

[12] A.F.M.A.U. Bhuiyan, Z. Feng, J.M. Johnson, H.L. Huang, J. Sarker, M. Zhu, M. R. Karim, B. Mazumder, J. Hwang, H. Zhao, Phase transformation in MOCVD

growth of (AlxGa1−x)2O3 thin films, Apl. Mater. 8 (2020), 031104, https://doi.org/10.1063/1.5140345.
[13] M. Fleischer, W. Hanrieder, H. Meixner, Stability of semiconducting gallium oxide thin films, Thin Solid Films 190 (1990) 93–102, https://doi.org/10.1016/0040-6090(90)90132-W.
[14] G.A. Battiston, R. Gerbasi, M. Porchia, R. Bertoncello, F. Caccavale, Chemical vapour deposition and characterization of gallium oxide thin films, Thin Solid Films 279 (1996) 115–118, https://doi.org/10.1016/0040-6090(95)08161-5.
[15] Y. Kokubun, K. Miura, F. Endo, S. Nakagomi, Sol-gel prepared β-Ga2O3 thin films for ultraviolet photodetectors, Appl. Phys. Lett. 90 (2007), 031912, https://doi.org/10.1063/1.2432946.
[16] A. Goyal, B.S. Yadav, O.P. Thakur, A.K. Kapoor, R. Muralidharan, Effect of annealing on β-Ga2O3 film grown by pulsed laser deposition technique, J. Alloys Compd. 583 (2014) 214–219, https://doi.org/10.1016/J.JALLCOM.2013.08.115.
[17] H. Li, S.H. Yuan, T.M. Huang, H.J. Chen, F.H. Lu, S. Zhang, D.S. Wuu, Impact of thermal-induced sapphire substrate erosion on material and photodetector characteristics of sputtered Ga2O3 films, J. Alloys Compd. 823 (2020), 153755, https://doi.org/10.1016/j.jallcom.2020.153755.
[18] A.K. Singh, S. Yadav, P.K. Kulriya, Y.S. Katharria, Sapphire substrate induced effects on β-Ga2O3 thin films, J. Mater. Sci. Mater. Electron. 33 (2022) 12629–12637, https://doi.org/10.1007/S10854-022-08212-X/FIGURES/9.
[19] M. Hilfiker, E. Williams, U. Kilic, Y. Traouli, N. Koeppe, J. Rivera, A. Abakar, M. Stokey, R. Korlacki, Z. Galazka, K. Irmscher, M. Schubert, Elevated temperature spectroscopic ellipsometry analysis of the dielectric function, exciton, band-to-band transition, and high-frequency dielectric constant properties for single-crystal ZnGa2O4, Appl. Phys. Lett. 120 (2022), 132105, https://doi.org/10.1063/5.0087623.
[20] C.C. Wang, S.H. Yuan, S.L. Ou, S.Y. Huang, K.Y. Lin, Y.A. Chen, P.W. Hsiao, D. S. Wuu, Growth and characterization of co-sputtered aluminum-gallium oxide thin films on sapphire substrates, J. Alloys Compd. 765 (2018) 894–900, https://doi.org/10.1016/J.JALLCOM.2018.06.270.
[21] P. Giannozzi, S. Baroni, N. Bonini, M. Calandra, R. Car, C. Cavazzoni, D. Ceresoli, G.L. Chiarotti, M. Cococcioni, I. Dabo, A. Dal Corso, S. De Gironcoli, S. Fabris, G. Fratesi, R. Gebauer, U. Gerstmann, C. Gougoussis, A. Kokalj, M. Lazzeri, L. Martin-Samos, N. Marzari, F. Mauri, R. Mazzarello, S. Paolini, A. Pasquarello, L. Paulatto, C. Sbraccia, S. Scandolo, G. Sclauzero, A.P. Seitsonen, A. Smogunov, P. Umari, R.M. Wentzcovitch, Quantum espresso: a modular and open-source software project for quantum simulations of materials, J. Phys. Condens. Matter 21 (2009), https://doi.org/10.1088/0953-8984/21/39/395502.
[22] D. Vanderbilt, Soft self-consistent pseudopotentials in a generalized eigenvalue formalism, Phys. Rev. B 41 (1990) 7892, https://doi.org/10.1103/PhysRevB.41.7892.
[23] M.I. Chen, A.K. Singh, J.L. Chiang, R.H. Horng, D.S. Wuu, Zinc gallium oxide—a review from synthesis to applications, Nanomaterials 10 (2020) 1–37, https://doi.org/10.3390/nano10112208.
[24] S. Luo, G.F. Harrington, K.-T. Wu, T. Lippert, Heteroepitaxial (111) ZnGa2O4 thin films grown on (00.1) sapphire by pulsed laser deposition, Phys. Status Solidi Rapid Res. Lett. 14 (2020), 2000270, https://doi.org/10.1002/pssr.202000270.
[25] W.H. Bragg, W.L. Bragg Apr, B.W. H Bragg, C. Professor of Physics, the reflection of X-rays by crystals, Proc. R. Soc. Lond. - Ser. A Contain. Pap. a Math. Phys. Character 88 (1913) 428–438, https://doi.org/10.1098/RSPA.1913.0040.
[26] Z. Galazka, S. Ganschow, R. Schewski, K. Irmscher, D. Klimm, A. Kwasniewski, M. Pietsch, A. Fiedler, I. Schulze-Jonack, M. Albrecht, T. Schröder, M. Bickermann, Ultra-wide bandgap, conductive, high mobility, and high quality melt-grown bulk ZnGa 2 O 4 single crystals, Apl. Mater. 7 (2019), 22512, https://doi.org/10.1063/1.5053867.
[27] R.-H. Horng, D.-S. Wuu, P.-L. Liu, A. Sood, F.-G. Tarntair, Y.-H. Chen, S.J. Pratap, C.-L. Hsiao, Growth mechanism and characteristics of β-Ga2O3 heteroepitaxailly grown on sapphire by metalorganic chemical vapor deposition, Mater. Today Adv. 16 (2022), 100320, https://doi.org/10.1016/j.mtadv.2022.100320.
[28] Y.S. Shen, W.K. Wang, R.H. Horng, Characterizations of metal-oxide-semiconductor field-effect transistors of ZnGaO grown on sapphire substrate, IEEE J. Electron Devices Soc. 5 (2017) 112–116, https://doi.org/10.1109/JEDS.2017.2653419.
[29] S. Luo, G.F. Harrington, K.T. Wu, D. Pergolesi, T. Lippert, Heteroepitaxial hexagonal (00.1) CuFeO2 thin film grown on cubic (001) SrTiO3 substrate through translational and rotational domain matching, Phys. Status Solidi Rapid Res. Lett. 15 (2021), 2100002, https://doi.org/10.1002/PSSR.202100002.
[30] S. Nakagomi, Y. Kokubun, Crystal orientation of β-Ga2O3 thin films formed on c-plane and a-plane sapphire substrate, J. Cryst. Growth 349 (2012) 12–18, https://doi.org/10.1016/J.JCRYSGRO.2012.04.006.
[31] H.G. Tompkins, E.A. Irene, Handbook of ellipsometry, Handb. Ellipsom (2005) 1–870, https://doi.org/10.1515/arh-2005-0022.
[32] J.M. Khoshman, J.N. Hilfiker, N. Tabet, M.E. Kordesch, Multiple oscillator models for the optical constants of polycrystalline zinc oxide thin films over a wide wavelength range, Appl. Surf. Sci. 307 (2014) 558–565, https://doi.org/10.1016/j.apsusc.2014.04.073.
[33] S. Bairagi, C.-L. Hsiao, R. Magnusson, J. Birch, J.P. Chu, F.-G. Tarntair, R.-H. Horng, K. Järrendahl, Zinc gallate (ZnGa 2 O 4) epitaxial thin films: determination of optical properties and bandgap estimation using spectroscopic ellipsometry, Opt. Mater. Express 12 (2022) 3284, https://doi.org/10.1364/ome.462668.
[34] C.M. Herzinger, B.D. Johs, Dielectric Function Parametric Model, and Method of Use, 1995.
[35] B. Johs, C.M. Herzinger, J.H. Dinan, A. Cornfeld, J.D. Benson, Development of a parametric optical constant model for Hg1−xCdxTe for control of composition by spectroscopic ellipsometry during MBE growth, Thin Solid Films 313–314 (1998) 137–142, https://doi.org/10.1016/S0040-6090(97)00800-6.
[36] D.E. Aspnes, Optical properties of thin films, Thin Solid Films 89 (1982) 249–262, https://doi.org/10.1016/0040-6090(82)90590-9.
[37] D.A.G. Bruggeman, Berechnung verschiedener physikalischer Konstanten von heterogenen Substanzen. I. Dielektrizitätskonstanten und Leitfähigkeiten der Mischkörper aus isotropen Substanzen, Ann. Phys. 416 (1935) 636–664, https://doi.org/10.1002/ANDP.19354160705.
[38] K. Levenberg1, F. Arsenal, A method for the solution of certain non-linear problems in least squares, Q. Appl. Math. 2 (1944) 164–168, https://doi.org/10.1090/QAM/10666.
[39] D.W. Marquardt, An Algorithm for Least-Squares Estimation of Nonlinear Parameters, 2006, pp. 431–441, https://doi.org/10.1137/0111030. Http://Dx.Doi.Org/10.1137/0111030. 11.
[40] M. Hilfiker, M. Stokey, R. Korlacki, U. Kilic, Z. Galazka, K. Irmscher, S. Zollner, M. Schubert, Zinc gallate spinel dielectric function, band-to-band transitions, and Γ-point effective mass parameters, Appl. Phys. Lett. 118 (2021), 132102, https://doi.org/10.1063/5.0043686.
[41] M. Hilfiker, U. Kilic, A. Mock, V. Darakchieva, S. Knight, R. Korlacki, A. Mauze, Y. Zhang, J. Speck, M. Schubert, Dielectric function tensor (1.5 eV to 9.0 eV), anisotropy, and band to band transitions of monoclinic β-(AlxGa1–x)2O3 ($x \leq 0.21$) films, Appl. Phys. Lett. 114 (2019), 231901, https://doi.org/10.1063/1.5097780.
[42] M. Hilfiker, R. Korlacki, R. Jinno, Y. Cho, H.G. Xing, D. Jena, U. Kilic, M. Stokey, M. Schubert, Anisotropic dielectric functions, band-to-band transitions, and critical points in α-Ga2O3, Appl. Phys. Lett. 118 (2021), 062103, https://doi.org/10.1063/5.0031424.
[43] E. Swinnich, Y.J. Dave, E.B. Pitman, S. Broderick, B. Mazumder, J.H. Seo, Prediction of optical band gap of β-(AlxGa1-x)2O3 using material informatics, Mater. Discov. 11 (2018) 1–5, https://doi.org/10.1016/J.MD.2018.06.001.